Accepted Manuscript

Journal of the Geological Society

Cooling and exhumation of the Late Paleozoic Tulasu epithermal gold system, Western Tianshan, NW China: implications for preservation of Pre-Mesozoic epithermal deposits

Xiao-Bo Zhao, Chun-Ji Xue, Wei-Ce Zhao, Reimar Seltmann, David T.A. Symons, Alla Dolgopolova & Yong Zhang

DOI: https://doi.org/10.1144/jgs2020-099

To access the most recent version of this article, please click the DOI URL in the line above.

Received 25 May 2020
Revised 10 October 2020
Accepted 22 November 2020

Cooling and exhumation of the Late Paleozoic Tulasu epithermal gold system, Western Tianshan, NW China: implications for preservation of Pre-Mesozoic epithermal deposits

Xiao-Bo Zhao[1], Chun-Ji Xue[1*], Wei-Ce Zhao[2], Reimar Seltmann[3], David T.A. Symons[4], Alla Dolgopolova[3] & Yong Zhang[1]

[1]State Key Laboratory of Geological Processes and Mineral Resources, Faculty of Earth Sciences and Resources, China University of Geosciences, Beijing 100083, China

[2]Beijing Institute of Geology for Mineral Resources Co., Ltd., Beijing 100012, China

[3]Center for Russian and Central Eurasian Mineral Studies, Department of Earth Sciences, Natural History Museum, Cromwell Road, London SW75BD, UK

[4]Department of Earth Sciences, University of Windsor, Windsor, ON N9B 3P4, Canada

[*]Correspondence: chunji.xue@cugb.edu.cn

Abstract: Epithermal gold deposits are rarely well preserved in pre-Mesozoic terranes because their low-temperature mineralization in shallow crust levels, and easily destroyed by subsequent erosion or depleted by tectonic events. However, several significant late Paleozoic epithermal gold deposits have been found in the Tulasu volcanic basin in NW China, forming one of the largest gold districts in the western Tianshan orogen. Here, we report new $^{40}Ar/^{39}Ar$ age from a monzonite porphyry enclave hosted in andesite and apatite fission track (AFT) data for 10 volcanic rocks from the Tulasu basin. These data, combined with the previous dataset, are used to perform inverse thermal modelling to quantify the district's cooling and exhumation history. Our modelling indicates a phase of burial reheating during late Paleozoic sedimentation following the mineralization, and subsequent a rapid exhumation in the Jurassic to Early Cretaceous (~196–128 Ma), and a slow exhumation until to present. The Mesozoic exhumation is likely related to the far-field effects of the Cimmerian orogeny along the southern Eurasian margin. Therefore, we suggest that the quick burial by thick sediments and the slow protracted exhumation after mineralization were crucial for the preservation of the Paleozoic epithermal gold system at Tulasu.

Introduction

Epithermal gold deposits form at shallow crustal levels of <1.5 km, low temperatures of <200 ℃ and low pressures of 10–50 MPa in volcanic arc or back-arc extensional settings (Hedenquist *et al*. 2000; Sillitoe & Hedenquist 2003). However, such conditions are generally

unfavorable for their preservation because of the long-term and intricate geological processes after mineralization (Simmons *et al.* 2005). As a result, most of the world's epithermal gold deposits are geologically young, such as the many Mesozoic and Cenozoic epithermal gold deposits in the circum-Pacific and the Tethyan belts (Corbett & Leach, 1998; Cooke and Simmons 2000; Kerrich *et al*., 2000), and the preservation of Pre-Mesozoic deposits is relatively rare. Nonetheless, exceptions exist in the Paleozoic western Tianshan Orogen, which lies in the southwestern Central Asian Orogenic Belt (Fig. 1A; Han *et al*. 2011). The orogen is well endowed with numerous pre-Mesozoic epithermal gold deposits that formed during late Paleozoic accretionary and collisional processes, including two representative epithermal gold systems: the Almalyk district in eastern Uzbekistan (overprinting a giant porphyry copper system) and the Tulasu volcanic basin in northwest China (Fig. 1B; Seltmann *et al*. 2014; Zhao *et al*., 2104*a*). However, these pre-Mesozoic epithermal gold deposits should probably have been wiped out by the complex and episodic Mesozoic to Cenozoic exhumation and erosion processes, as revealed by previous thermochronological studies (Glorie & De Grave 2016; Jepson *et al*. 2018; Zhang *et al*. 2019). How did these pre-Mesozoic epithermal gold deposits survive the exhumation and erosion processes of the ancient orogenic belt? This question remains enigmatic and requires a thorough understanding.

The Tulasu volcanic basin is located ~30 km northeast of Yining City (Fig. 1B), and it hosts several important Paleozoic epithermal gold deposits, i.e., Axi, Tawuerbieke and Qiabukanzhuota (Hart *et al*. 2003; Pirajno *et al*. 2011; Zhao *et al*. 2014*a*; Gu *et al*. 2016). The basin's exploration history can be traced back to the late 1980s when the No. 1 Geological Team of the Xinjiang Bureau of Geology and Mineral Resources carried out a 1: 50000 litho-stratigraphic mapping and geochemical investigation to successively discover the three deposits (XJBGR 1993). Since then, multidisciplinary research projects have sought to unravel the metallogenesis of this large epithermal gold district by the study of the deposits' geology and geochemistry (e.g., Zhai *et al*. 2009; Zhao *et al*. 2014*b*; Gu *et al*. 2016; An & Zhu 2018), petrology (e.g., An *et al*. 2013; Tang *et al*. 2009; Yu *et al*. 2016; Zhao *et al*. 2020), mineralogy (e.g., Liu *et al*. 2018; Zhang *et al*. 2018) and geochronology (e.g., Zhao *et al*. 2014*c*; Peng *et al*. 2017; Liu *et al*. 2019). So far, these studies have ignored to address the crucial question of the epigenetic district's post-mineralization exhumation history and its preservation mechanism.

Apatite fission track (AFT) dating is one of the most widely used low-temperature thermochronological techniques, and it has been widely applied in economic geology to reconstruct the post-mineralization history of a deposit (McInnes *et al*. 2005). Due to its

thermal sensitivity to low temperatures (~60–120 °C; Gallagher *et al*. 1998), AFT dating can help to elucidate the low-temperature thermal history and exhumation process of an epithermal deposit, as well as help to estimate its preservation potential (McInnes *et al*. 2005). In this contribution, we applied the AFT technique with the $^{40}Ar/^{39}Ar$ dating method and numerical modelling both to better quantify the cooling and exhumation history of the late Paleozoic Tulasu epithermal gold district and to provide new insights into the preservation of pre-Mesozoic epithermal gold deposits in ancient orogenic belts.

Geological Setting

The 2000-km-long western Tianshan orogeny experienced multiple Paleozoic subduction, accretion and collision events that involved complex geodynamic interactions between several branches of the Paleo-Asian Ocean, including the Terskey, Turkestan and Junggar oceans (Windley *et al*. 2007; Biske & Seltmann 2010; Xiao *et al*. 2013, 2015; Han & Zhao 2018). During the Mesozoic and Cenozoic, the ancestral orogen was modified by the intense reactivation from intracontinental deformation, episodic uplift and exhumation processes that reworked this magnificent mountain range (Jolivet *et al*. 2010; Glorie & De Grave 2016; Jepson *et al*. 2018; Wang *et al*. 2018; Zhang *et al*. 2019). Bounded by the Nikolaev Line–North Nalati and the Turkestan–Atbashi–Inylchek fault zones, the western Tianshan orogen is generally divided into the North, Middle and South Tianshan tectonic units (Fig. 1A; Zonenshain *et al*. 1990; Biske & Seltmann 2010; Xue *et al*. 2014). These units are dextrally crosscut by the Talas–Fergana fault.

The North Tianshan comprises mainly Precambrian metamorphic basement with overlying Paleozoic volcanic and sedimentary formations (Mikolaichuk *et al*. 1997; Gao *et al*. 1998; Xue *et al*. 2014). The northward subduction of the Terskey Ocean beneath the North Tianshan occurred in the Late Ordovician, followed by the accretion of Middle Tianshan to North Tianshan, which gave rise to the Nikolaev Line–North Nalati fault zone (Lomize *et al*. 1997; Glorie *et al*. 2010; Xue *et al*. 2014). To the west of Talas–Fergana fault, the Uzbekistan Middle Tianshan is represented by the late Paleozoic Beltau–Kurama arc belt that developed on the Precambrian basement and overlying Early Paleozoic clastic rocks (Seltmann *et al*. 2014). The Middle Tianshan narrows to the east and it contains a Precambrian basement and overlying Paleozoic volcanic–sedimentary sequence (Han & Zhao 2018; Zhao *et al*. 2019). Intense magmatism occurred in the Middle Tianshan that concentrated in the Silurian–Early Devonian and Late Carboniferous–Early Permian in response to the northward subduction and closure of the Turkestan Ocean, respectively (Han *et al*. 2011; Han & Zhao 2018). The South Tianshan represents a late Paleozoic accretionary belt that has experienced intense

thrusting and folding during the closure of the Turkestan Ocean (Biske & Seltmann 2010; Xiao *et al*. 2013).

Tectonically, the Tulasu epithermal gold district occurs in the western part of the Chinese North Tianshan (Fig. 1B). The gold deposits are hosted by a fault-controlled volcanic–sedimentary basin that developed on a continental arc which formed from the southward subduction of the Junggar Ocean beneath the North Tianshan during the late Paleozoic (Chen *et al*. 2011; Xiao *et al*. 2013; Zhao *et al*. 2014*a*). The Junggar Ocean is suggested to have opened as early as the Late Cambrian (Ren *et al*. 2014; 2018b), and the Bayingou and Lucaogou ophiolitic mélanges along the northern edge of Chinese North Tianshan are thought to be the remnants of the Junggar oceanic crust (Xu *et al*. 2006). The ocean is believed to have been still active in the Early Carboniferous, as evidenced by the Late Devonian conodonts and Early Carboniferous radiolarians found in the siliciclastic rocks of the Bayingou mélange (Xiao *et al*. 1992), and by zircon U–Pb ages of 325 ± 7 Ma and 344 ± 3 Ma found for the cumulate gabbro and plagiogranite (Xu *et al*. 2006), respectively. The southward subduction of the Junggar Ocean led to the development of the Devono-Carboniferous northern Yili arc (Wang *et al*. 2006). The closure of the ocean led to the formation of the North Tianshan Fault, and is dated by the Sikeshu stitching intrusion that gives a SHRIMP zircon U–Pb age of 316 ± 3 Ma (Han *et al*. 2011). During the Permian, intense intracontinental dextral shearing occurred along the North Tianshan Fault (Wang *et al*. 2006), and an Early Permian exhumation event is recognized by recent AFT data in the North Chinese Tianshan (Wang *et al*. 2018). The Mesozoic and Cenozoic in the North Tianshan are characterized by multiple crustal uplift and exhumation events that mainly occurred in the Late Triassic–Cretaceous and Late Cenozoic (Glorie *et al*. 2010; De Grave *et al*. 2013; Zhang *et al*. 2019).

Geology of the Tulasu Epithermal Gold District

The Tulasu volcanic basin hosts the large Axi and Jingxi-Yelmend gold deposits, the small-sized Tawuerbieke and Qiabukanzhuota gold deposits, as well as the Tabei lead–zinc and the Tieliekesayi dickite prospects that constitute a late Paleozoic epithermal gold system (Zhao *et al*. 2014*a*; Gu *et al*. 2016). The system is bounded by the regional NW–SE-striking North Yili Basin Fault and WNW–ESE-striking South Keguqin Fault, and its structural framework is characterized by a number of faults with different orientations (e.g., N–S, NW–SE and NE–SW). In the basin, the Ordovician–Silurian marine clastic rock and carbonate rock are locally exposed with interlayered volcanoclastic rock. They are unconformably overlain by an Lower Devonian molasse succession (Fig. 2), which are unconformably

overlain in turn by terrestrial arc-related volcanic rocks of the Lower Devonian to Lower Carboniferous Dahalajunshan Formation (Fig. 3), shallow marine carbonates and clastic rocks of the Aqialehe Formation (~840–2180 m thick) and volcanoclastic rocks of the Upper Carboniferous Naogaitu Formation (~1410–1920 m thick; XJBGR 1993), respectively.

The Dahalajunshan volcanic Formation (DVF) are the main host rocks of the Tulasu epithermal gold system (Fig. 2). The strata are commonly gently to medium dipping and they are divided into five lithological members (Fig. 3), which from bottom to top are the (1) Conglomeratic Member (> 150 m thick), (2) Acidic Tuff Member (> 150 m thick), (3) Lower Andesite Member (170–210 m thick), (4) Volcanoclastic Member (470–540 m thick) and (5) Upper Andesite Member (> 530 m thick; XJBGR 1993; Zhai *et al*. 2009). At Axi, Zhai *et al*. (2009) and An *et al*. (2013) have reported zircon SHRIMP U–Pb ages of 363.2 ± 5.7 Ma and 356.2 ± 2.0 Ma for the andesite, respectively. At Tawuerbieke, zircons from the andesite have yielded a LA–ICP–MS U–Pb age of 347.2 ± 1.6 Ma (Tang *et al*. 2009) and SHRIMP U–Pb ages of 360.5 ± 3.4 Ma (Zhao *et al*. 2014*b*) and 367.1 ± 3.2 Ma (Peng *et al*. 2017). An Early Carboniferous granitic porphyry in the Tawuerbieke deposit has given a zircon LA–ICP–MS U–Pb age of 349 ± 2 Ma (Tang *et al*. 2013) and a SHRIMP U–Pb age of 355.4 ± 4.0 Ma (Zhao *et al*. 2014a). In addition, a monzonite porphyry enclave found in the andesite at Tawuerbieke has yielded a zircon SHRIMP U–Pb age of 356.2 ± 4.3 Ma, and it is believed to be homologous with the andesite (Zhao *et al*. 2014*c*). An *et al*. (2013) reported zircon SHRIMP U–Pb ages of 386.4 ± 9.3 Ma and 416.7 ± 2.6 Ma, respectively, for rhyolite and tuff from the bottom of the DVF at the northwest margin of the Tulasu basin (ca. Jingxi-Yelmend), whereas subvolcanic porphyritic andesite from this area has an U–Pb SHRIMP age of 370.5 ± 2.1 Ma (An *et al*. 2014) (Fig. 3).

Systematic descriptions for the main characteristics of gold deposits in the Tulasu epithermal gold district have been summarized in Zhao *et al*. (2014*a*), for which a brief introduction is presented below and listed in Table 1. The large Axi deposit is the most representative epithermal gold deposit in the Tianshan Orogen, containing ~70 t gold at an average grade of ~5.57 g/t (Rui *et al*. 2002). It was the first major gold discovery at Tulasu in 1989, followed later by the Tawuerbieke and Qiabukanzhuota gold deposits (XJBGR 1993). Exploration at Axi was completed by 1995 with subsequent open-pit mining and then underground mining in 2004. The Axi deposit is hosted by volcanic rocks of the Upper Andesite member of the DVF, and its lenticular orebody is dominated by a series of annular and radial faults, especially a N–S-striking fault (Fig. 2). The deposit shows a clear alteration zonation from the center of the orebody outwards, including silicification, phyllic and

propylitization zones (Zhai *et al*. 2009). Recently, Liu *et al*. (2019) reported two Re–Os isochron ages of 350 ± 10 Ma and 332 ± 8 Ma for pyrites from the sericite-quartz altered ores and from later grey quartz veins, respectively, which indicate two distinct stages of gold mineralization at Axi. Gold orebodies at Tawuerbieke occur as veins and lenses in the granitic porphyry and andesite of the Upper Andesite member of the DVF. The Early hydrothermal alteration stage consists of silicification, sericitization and carbonatization processes and led to the formation of altered rock ores, on which were superimposed by the late calcite–quartz vein ores. Re–Os dating on gold-bearing pyrite from the auriferous veins yielded an isochron age of 323 ± 11 Ma (Zhao *et al*. 2014*b*). The Qiabukanzhuota gold prospect is hosted in dacite and tuff of the DVF, and the orebody occurs mainly as lenses along interlayer fracture zones to form the breccia and massive ores. The Tabei Lead–Zinc prospect is hosted in the Upper Andesite member of the DVF and it is also dominated by the N–S-striking fault (Gu *et al*. 2016). Mineralization at Tabei can be divided into three types, namely breccia, massive and disseminated ores (Zhao *et al*. 2014*a*).

Sampling and Analytical Methods

Sample preparation

A total of ten unaltered samples of the DVF were collected from different stratigraphic elevations in the Tulasu volcanic basin (Table 2; Figs. 2 and 3), including andesite (# N-1, S-2, S-5 and S-6), basaltic andesite (# D-1 and Y-1), tuff (# N-2 and QBK-1), dacite (# S-7) and rhyolite (# Y-11). Apatite grains were hand-picked out from these samples for fission track observation, measurement and dating. One sample from a monzonite porphyry enclave (# XT4-8) in andesite, which has undergone later sericite alteration (Zhao *et al*. 2014c), was collected from the Tawuerbieke deposit and K-feldspar grains were chosen for $^{40}Ar/^{39}Ar$ dating (Table 2; Fig. 2). The K-feldspar and apatite grains were separated from the crushed rocks by using a combination of magnetic and heavy liquid separation techniques, and then individual grains were handpicked under a binocular microscope. Table 2 gives a summary of lithology, sampling coordinates and elevation, and dated mineral for the samples.

$^{40}Ar/^{39}Ar$ dating

The $^{40}Ar/^{39}Ar$ analysis was conducted at the Institute of Geology, Chinese Academy of Geological Sciences (CAGS). The sample grains were ultrasonically cleaned with ethanol, and then they were sealed into a quartz bottle for irradiation in the Swimming Pool Reactor, Chinese Institute of Atomic Energy, Beijing, along with the ZBH-25 biotite standard with an age of 132.7 ± 1.2 Ma at 1σ and a potassium content of 7.6 wt. % (Wang 1983). The duration

of irradiation was 1440 minutes with a neutron flux of 2.65×10^{13} n/cm^2 and an integrated neutron flux of 2.29×10^{18} n/cm^2. After irradiation, the sample was stepwise heated from 700 ℃ to 1400 ℃ with each step lasting for 10 minutes, followed by a 20-minute purification. Finally, the isotopic analysis was performed by using a Helix multiple collector mass spectrometer. The measured isotopic ratios were corrected for system blanks, mass discrimination, interference isotopes and atmospheric argon. The interference isotope correction factors were calculated from co-irradiation of pure salts of K_2SO4 and CaF_2, i.e., $(^{40}Ar/^{39}Ar)_K = 0.004782$, $(^{39}Ar/^{37}Ar)_{Ca} = 0.000806$ and $(^{36}Ar/^{37}Ar)_{Ca} = 0.0002398$. All ^{37}Ar abundances were corrected for radiogenic decay. The decay constant was 5.543×10^{-10} year^{-1} (Steiger & Jäger 1977). The $^{40}Ar/^{39}Ar$ plateau age with its ± 2σ error was calculated using the ArArCALC program (Koppers 2002). The detailed procedure has been reported by Chen *et al*. (2002).

Fission track measurement

The apatite fission track measurement was conducted at the Institute of Geology, China Earthquake Administration (IGCEA). The detailed analytical procedure is given by Pang *et al*. (2013) and it is briefly introduced here. Apatite grains without fractures and inclusions were dated using a uranium-poor muscovite sheet as an external detector (Gleadow 1981). The apatite grains were coated with either Teflon or epoxy resin, followed by polishing. Subsequently, the Teflon-coated grains were etched in a KOH–NaOH eutectic melt at 228 ℃ for 19 hours and the epoxy resin-coated grains were etched in a 40% 5 mol/L HNO_3 solution at room temperature for 18 minutes. The neutron flux was monitored using CN5 uranium dosimeter glasses. Next, the tracks on the muscovite detectors were revealed by etching in a concentrated HF solution at room temperature. The track densities of the natural apatite grains (ρ_s), the induced fission track populations on the muscovite external detector (ρ_i) and the monitor dosimeter glasses (ρ_d) were measured at 1000× magnification on screen photos from an Olympus microscope, as were the lengths of confined tracks parallel to the C-axis. The fission track ages, which are reported with the ±1σ error, were determined based on the zeta (ζ) calibration using a standard weighted mean zeta of 356.6 ± 10 (Hurford & Green 1983). Only horizontally-confined tracks were measured for the grains that are confined in the grain and running parallel to the grain's surface. The chi-square (χ^2) test was used to quantify the homogeneity of the ages (Galbraith 1981). Samples with a chi-squared probability of > 5%, i.e., $P(\chi^2) > 5\%$, indicate a single age population. For samples with a chi-squared probability of < 5%, the binomial peak fitting method was applied to decompose the observed age distribution into its best–fitting grain age components.

Results

K-feldspar $^{40}Ar/^{39}Ar$ age

The K-feldspar $^{40}Ar/^{39}Ar$ age dating results from sample XT4-8 are given in Table 3 and the corresponding plateau-age spectrum is shown in Figure 4. Seven high-temperature steps from 820 °C to 1140 °C yield a well-defined K-feldspar $^{40}Ar/^{39}Ar$ plateau age of 313.5 ± 2.2 Ma (2σ; MSWD = 0.82) with ~54.6% of the released ^{39}Ar accumulated (Table 3; Fig. 4).

Apatite fission track data

The AFT ages are presented in Table 4, and the distribution of the single grain ages for each sample are depicted on radial plots in Figure 5 (Galbraith & Laslett 1993). For all samples, 35 apatite grains were dated, except for sample Y-1 where 19 apatite grains were dated. Sample S-2 failed the χ^2 test, giving a P(χ^2) value of 1.2%, which is < 5.0% (Table 4), and the central age is chosen as its AFT age. All other samples pass the χ^2 test (Table 4), indicating a single cooling history, and the pooled grain ages are interpreted to be the respective sample AFT ages. Thus, 10 samples yielded Late Jurassic to Early Cretaceous AFT ages, ranging from 156 ± 11 Ma to 109 ± 8 Ma (1σ) (Table 4). The mean track lengths of the samples range from 11.8 ± 2.1 to 13.2 ± 2.4 μm (Table 4; Fig. 6), which are apparently less than the original track lengths of 16.3 ± 0.9 μm (Gleadow *et al.* 1986) and the mean length of rapid cooling tracks of 14.5–15.5 μm (Green *et al.* 1989), indicating slow cooling with a protracted residence in the apatite partial annealing zone (APAZ) for the samples.

Inverse Thermal Modelling

The AFT age and length data were analyzed using the HeFTy inverse modeling program (version 1.9.1; Ketcham 2005) to better understand the thermal history of the Tulasu epithermal gold system. Samples with less than 40 confined fission tracks may cause ambiguous thermal models (Barbarand *et al.* 2003), and thus samples Y-1 and Y-11 were excluded from the modeling. Sample N-1 was also excluded due to its inadequate Dpar data. The apatite annealing equations of Ketcham *et al.* (2007) was preferentially chosen as the annealing model, and accordant option was automatically selected for the C-axis projection. The initial mean track length was set to be 16.3 μm by default (Gleadow *et al.* 1986), and the Dpar values of fission tracks from each sample were used as kinetic parameters for the modelling. The modelling relies on the Monte Carlo simulation to generate statistically acceptable time–temperature paths (Ketcham 2005). Before running the simulation, it requires several vital time–temperature constraints to better define the thermal history. Since

all the samples yielded Late Jurassic to Early Cretaceous AFT ages that are distinctly younger than the Late Devonian to Early Carboniferous eruptive ages, the samples must have experienced at least one episode of total annealing after eruption, which in turn suggests that all samples must have been totally annealed at temperatures above 120 °C before the apatite grain with oldest fission track age entered the APAZ. Ages older than the oldest fission track age of each sample and temperatures higher than 120 °C were set as the initial time and temperature constraints for modelling. Thus, the AFT ages of the samples were required to be in the APAZ range (~60–120 °C; Gallagher *et al*. 1998), which were set as another pair of time and temperature constraints. Further, only paths within the APAZ can be validly interpreted because the fission tracks in apatite anneal instantaneously at temperatures above ~120 °C and the annealing rate becomes extremely slow for temperatures below ~60 °C (Jolivet *et al*. 2010). The terminal time and temperature constraints of the modelling were set as 0 Ma and current surface temperature assuming to be ~20 °C, because all the samples were collected from the surface.

The results of the modelling are expressed as time–temperature path envelopes, as shown in Figure 7. The purple and pale purple envelopes encompass all the good paths with a goodness-of-fit of > 0.50 and all of the acceptable paths with a goodness-of-fit of > 0.05, respectively. The weighted mean path (colored line) is estimated to be the likeliest thermal history for each sample (Fig. 7). In general, the modelled time–temperature paths indicate similar protracted cooling history (Fig. 7). Sample D-1 crossed the 120 °C isotherm at ~196 Ma in a phase of relatively fast cooling at a rate of ~1.4 °C/Ma that took it to the upper part of APAZ (~70 °C) at ~156 Ma (Fig. 7; D-1). The sample then followed an isothermal phase at a rapidly decreased rate of ~0.1 °C/Ma from ~156 Ma to ~98 Ma, after which it cooled at a rate of ~0.5 °C/Ma to pass extremely slowly through the upper limit of the APAZ at ~84 Ma (Fig. 7; D-1). Samples N-2 and S-2 entered the APAZ at ~188 Ma and ~174 Ma, respectively, and both left it at ~95 ± 2 Ma (Fig. 7; N-2 and S-2). The cooling paths show gently decreasing rates from ~0.9 °C/Ma to ~0.4 °C/Ma and from ~1.1 °C/Ma to ~0.5 °C/Ma, respectively. The other four samples share similar two-phase cooling paths with fast cooling at rates of ~1.3–2.7 °C/Ma and extremely slow cooling at rates of ~0.4–0.5 °C/Ma (Fig. 7; S-5, S-6, S-7 and QBK-1). The decreasing of the cooling rates occurred mostly in the upper APAZ (~75–90 °C). These four samples successively crossed the 120 °C isotherm from ~175 to 138 Ma and left the APAZ from ~105 to 85 Ma (Fig. 7).

Discussion

Cooling and exhumation of the Tulasu epithermal gold system

Our new K-feldspar $^{40}Ar/^{39}Ar$ and apatite fission track data are combined with previous geochronological ages to reconstruct the cooling and exhumation history of the Tulasu epithermal gold system (Fig. 8). The peak of the volcanism (DVF) hosting epithermal gold deposits in the Tulasu basin concentrating to Late Devonian–Early Carboniferous according to previous zircon U–Pb data (~367.1–347.2 Ma; Zhai *et al*. 2009; An *et al*. 2013; Tang *et al*. 2009; Zhao *et al*. 2014*c*, 2020; Peng *et al*. 2017). Once the volcanic rocks were erupted to the surface, they cooled instantaneously from ~900 ℃ (the closure temperature of the zircon U–Pb system; Cherniak & Watson 2001) to the paleo-surface temperature of ~20 ℃ (Fig. 8).

The K-feldspar $^{40}Ar/^{39}Ar$ system has a broad range of closure temperatures between 350 ℃ and 150 ℃ because of its poorly quantified diffusion kinetics that result from complex internal microstructures in the K-feldspar crystal (McDougall & Harrison 1999). Hence, our $^{40}Ar/^{39}Ar$ age of K-feldspar for the monzonite porphyry enclave in andesite reveal a phase of reheating from ~357 Ma to ~315 Ma (Fig. 8) as the samples were gradually reheated to 150–350 ℃ in the Late Carboniferous, which resulted in the total annealing process of fission tracks in the apatite grains. Later magmatic event cannot be responsible for the reheating because there is no evidence for post-Carboniferous magmatism in the Tulasu basin. The two possible mechanism responsible for the reheating process includes basin subsidence with quick burial, and hydrothermal event.

The DVF are immediately unconformably overlain by the ~2.4–4.1 km thick Aqialehe and Naogaitu formations after a short period of erosion (Fig. 8). However, this thickness of cover rocks alone cannot reheat the samples to 150–350 ℃ if we adopt a geothermal gradient of ~25 ℃/km that is the norm for a sedimentary basin. A factor to be taken into account is basin subsidence with exposure to higher thermal gradients as is widely reported from post-orogenic transtensional to extensional strike-slip pull apart molasse basins. Similarly, Wainwright *et al*. (2017) reported from the Oyu Tolgoi (Mongolia) porphyry district the occurrence of Upper Devonian sedimentary rocks positioned stratigraphically above ~370 Ma copper-gold mineralization that preserve a record of uplift, exhumation, and subsequent burial shortly after mineralization. Preservation examples related to rapid subsidence and burial with high heat flow forming anthracitic coal in the Permo-Carboniferous Erzgebirge basin (Germany) and with protracted exhumation across the Variscan molasse basins are elaborated by Wolff *et al*. (2015), Schneider & Romer (2010), Schneider *et al.* (2005) and Ventura & Lisker (2003).

Hot hydrothermal fluids flowing from depth are another probable cause of reheating. The sample collected at Tawuerbieke (# XT4-8) has indeed undergone later sericite alteration as have been described in Zhao *et al.* (2014c), which supports the occurrence of later

hydrothermal event. Further, a previous study of fluid inclusions in the gold-bearing quartz veins from the Axi gold deposit indicated that the ore-forming fluids originated from meteoric water and that fluid boiling occurred during the epithermal mineralization (Zhai *et al*. 2009). The meteoric water circulation drove hot hydrothermal fluids upwards through faults and thus reheated the samples to a temperature of 150–350 °C. Since the Carboniferous, the samples underwent a protracted cooling prior to cooling through the APAZ (~60–120 °C; Gallagher *et al*. 1998) during the Jurassic and Early Cretaceous before eventually reaching the present surface temperature (~20 °C; Fig. 8).

Our AFT data and thermal models reveal a Mesozoic exhumation history for the Tulasu epithermal gold system, which indicates that the samples underwent a phase of rapid exhumation at rates of ~0.029–0.091 mm/y during the Jurassic to Early Cretaceous (Fig. 7). This is also consistent with the geological evidence of thick Jurassic to Early Cretaceous detrital sediments occurred along the northern Yili basin (Glorie *et al*. 2010; Jolivet *et al*. 2010, 2013). The AFT ages of ~155–109 Ma fall in the range of previous Mesozoic AFT ages of mostly ~180–100 Ma in the western Tianshan, and they are thought to record a significant phase of cooling related to the far-field effects of the Cimmerian orogeny along the southern margin of the Eurasian continent and/or the closure of Mongol–Okhotsk Ocean (De Grave *et al*. 2007; Glorie *et al*. 2010; Jolivet *et al*. 2010; Jepson *et al*. 2018; Zhang *et al*. 2019). Available data suggest an eastward propagating, scissor-like closure of the Mongol–Okhotsk Ocean over a period from the Late Triassic to Early Cretaceous (Yang *et al*. 2015; Ren *et al*. 2018a). The closure of the western segment of the ocean is thought to be responsible for the Middle to Late Triassic/Early Jurassic cooling event in the western Tianshan (Glorie & De Grave 2016; Wang et al. 2018), while the closure of its eastern segment is suggested to have induced the Late Jurassic to Early Cretaceous exhumation of the western Tianshan (De Grave et al. 2007; Glorie & De Grave 2016). However, Jolivet *et al*. (2010) argued that the Late Jurassic to Early Cretaceous exhumation in the western Tianshan cannot be correlated to the final closure of the Mongol–Okhotsk Ocean because the deformation events during this period does not exist in the Gobi Altai in Mongolia, which is spatially closer to the Mongol–Okhotsk Ocean. The Cimmerian orogeny involves successive evolution of the Tethyan oceanic basins from the Late Triassic to Early Cretaceous, leading to a series of accretionary and collisional events of several Cimmerian blocks, e.g. the Qiangtang and Lhasa blocks (Yin & Harrison, 2000; De Grave *et al*. 2007; Glorie *et al*. 2010). In particular, the Late Jurassic to Early Cretaceous accretion of the Lhasa block into the southern Eurasian margin is more likely to become a far-field driving force for the Mesozoic exhumation at Tulasu due to their consistency in time. The Late Triassic to Early Jurassic

accretion of the Cimmerian Qiangtang block is often interpreted as the lure of the Middle to Late Triassic/Early Jurassic cooling event in the western Tianshan (Jolivet *et al*. 2010; Glorie & De Grave 2016; Jepson *et al*. 2018). Therefore, we suggest that the rapid exhumation in the Tulasu basin during the Jurassic to Early Cretaceous is most likely formed from far-field effects of the Cimmerian orogeny.

It is noteworthy that the sample QBK-1 yielded the youngest AFT age (109 ± 8 Ma) while corresponds to the highest elevation (2011 m; Table 2; Fig. 9). Theoretically, when there exists a regional horizontal isothermal surface, the AFT ages of the samples should be positively correlated with their elevations, which means that the sample with older AFT age should pass through the APAZ earlier to reach a higher elevation (Gleadow 1981). However, this is not the case at the Tulasu basin. After discarding this sample (# QBK-1), the other samples still display a slight negative correlation between the AFT ages and elevations (red dashed line in Figure 9). This negative linear relationship indicates that the isothermal surface was not horizontal at Tulasu, and differential distribution of thermal state may have existed to affect the AFT ages in the area (Gleadow 1981).

No Cenozoic AFT ages were obtained, indicating that no significant exhumation occurred in the basin, and our modelling showed a steady and protracted phase of slow exhumation at rates of ~0.013–0.018 mm/y after this rapid mid-Mesozoic exhumation (Fig. 8). The western Tianshan indeed remained tectonically stable in the Late Cretaceous, which induced extensive planation (De Grave *et al*. 2007; Jolivet *et al*. 2013; Chen *et al*. 2017). However, significant Cenozoic rapid cooling occurred in the western Tianshan as a remote response to India–Eurasia collision, and it has been commonly recorded by numerous thermochronological studies (Glorie *et al*. 2010; Glorie & De Grave 2016; Jepson *et al*. 2018; Zhang *et al*. 2019). Specifically, in the Keguqin mountain region, which was separated from the Tulasu basin by the South Keguqin Fault, AFT dating of granites has indicated Oligocene to Miocene exhumation (Wang *et al*. 2018). The South Keguqin Fault was formed in the Mesoproterozoic and it was reactivated by early Mesozoic normal faulting and by late Cenozoic thrusting, which were responsible for Late Triassic to Late Jurassic exhumation and rapid Oligocene to Miocene exhumation, respectively (XJBGR 1993; Wang *et al*. 2018). Thus, multiple reactivations of this basement fault may be responsible for differential exhumation between the Keguqin mountain and Tulasu basin.

Implications for the preservation of pre-Mesozoic epithermal deposits

The epithermal gold mineralization in the Tulasu basin is thought to be Early Carboniferous from direct Re–Os dating on gold-bearing pyrite (Zhao *et al*. 2014*b*; Liu *et al*. 2019).

Previous micro-thermometric data for fluid inclusions in the gold-bearing quartz veins revealed low temperatures (~120–240 ℃) and shallow mineralization depths (~700 m) for the gold mineralization, which is also supported by field geological evidence (Zhai *et al.* 2009; An & Zhu 2018; Liu *et al.* 2018). Such conditions seem to be very unfavorable for preservation of the mineralization, especially since erosion occurred immediately after gold mineralization as shown by the unconformity between the Dahalajunshan and Aqialehe formations although typomorphic characteristics of pyrite at Axi indicate minimal erosion (Wei *et al.* 2011). Our thermochronological study provides important information on the post-mineralization history at Tulasu to help understanding its preservation mechanism. Since the genesis of the epithermal mineralization, the Tulasu basin has undergone a phase of burial reheating until ~315 Ma despite the minor erosion by the unconformity event. The mineralization was covered by the Lower Carboniferous Aqialehe Formation and Upper Carboniferous sediments with total thickness of at least ~3.0 km (XJBGR 1993). Thick cover rocks drove the samples deep to generate the total annealing of apatite fission tracks, and more importantly, they protected the gold deposits from being eroded away. Although a phase of rapid exhumation at rates of ~0.029–0.091 mm/y occurred in the basin during the Jurassic to Early Cretaceous (Fig. 8), these rates are relatively slow over a geological time scale, and the resulting erosion of an estimated thickness of ~2.1 km was not enough to remove the deposits. Therefore, we suggest that rapid post-mineralization burial by a thick sequence of cover rocks and their subsequent relatively slow exhumation favored the preservation of the late Paleozoic Tulasu epithermal gold system.

The world's epithermal gold systems are concentrated in the circum-Pacific, Tethyan–Himalayan and Paleo-Asian metallogenic domains. Most of these systems are known to occur in Mesozoic or Cenozoic terranes (Cooke & Simmons 2000; Kerrich *et al.* 2000; Simmons *et al.* 2005), with a few pre-Mesozoic systems that are mainly found in the western Tianshan (Seltmann *et al.* 2014), Tasman (Corbett & Leach 1998) and Uralian (Lehmann *et al.* 1999) orogens. In the Tasman orogen, the Late Devonian Yerranderie silver–gold–lead district is hosted in the Early Devonian Bindook Volcanic Complex and it was covered by the Upper Devonian and Permian sediments after its deposition (Downes 2007). The Carboniferous Pajingo gold deposit was buried by overlying Permian–Triassic sediments following its epithermal mineralization in Late Devonian–Carboniferous volcanic rocks (Bobis *et al.* 1995). In the southern Ural orogen, the Bereznjakovskoje gold trend is hosted in Late Devonian volcanic–subvolcanic rocks, which are overlain by an Upper Devonian to Lower Carboniferous volcano-sedimentary sequence (Lehmann *et al.* 1999). Thus, it seems that a thick sequence of cover rocks was a vital factor in the preservation of these pre-Mesozoic

epithermal deposits by protecting the mineralization from erosion. Our study on the Tulasu epithermal gold system suggests further that a protracted slow exhumation with coeval tectonic stability also play important roles in preventing such epithermal deposits from being destroyed.

Conclusion

New $^{40}Ar/^{39}Ar$ and fission track data, when combined with previous geochronological data and inverse thermal modelling, constrain the cooling and exhumation history of the Tulasu epithermal gold system. The AFT ages of 10 volcanic rock samples range from 156 ± 11 Ma to 109 ± 8 Ma, and $^{40}Ar/^{39}Ar$ dating of K-feldspar in a monzonite porphyry enclave in andesite yields a plateau age of 313.5 ± 2.2 Ma. Thermal modelling shows a phase of reheating of the Early Carboniferous epithermal gold mineralization prior to ~315 Ma in the Tulasu basin that was likely caused by burial by younger Carboniferous sediments. The Tulasu basin then underwent a phase of rapid cooling at rates of ~0.9–2.7 ℃/Ma during the Jurassic to Early Cretaceous, followed by slow cooling at ~0.4–0.5 ℃/Ma. Rapid exhumation at rates of ~0.029–0.091 mm/y occurred in the Jurassic to Early Cretaceous, leading to an estimated ~2.1 km of erosion that was not enough to destroy the known epithermal deposits. We propose that syn- to post-mineralization basin subsidence and the rapid burial by thick cover rocks and the subsequent protracted slow exhumation appear to be pivotal factors in the preservation of the Tulasu epithermal gold system, similar to most of the pre-Mesozoic epithermal deposits worldwide.

Acknowledgements We are grateful to the officers and geologists of the Axi and Tawuerbieke deposits for access permission and logistical support. We thank three anonymous reviewers for constructive comments and Wenjiao Xiao for editorial handling. Also, we thank the staffs from the Institute of Geology, China Earthquake Administration and the Institute of Geology, Chinese Academy of Geological Science for providing technical assistance with the thermochronological analyses.

Funding This work was financially supported by the National Key R & D Program of China (2017YFC0601202), the National Natural Science Foundation of China (41602076) and the Fundamental Research Funds for the Central Universities (2652019044). This is a contribution to IGCP 662 Project “Orogenic Architecture and Crustal Growth from Accretion to Collision” under the patronage of UNESCO-IUGS.

Author contributions XBZ: principal investigator of the study and lead author drafting key parts of this manuscript; CJX: project leader co-funding, coordinating and supervising the initial study, contributing to manuscript chapters; WCZ: Co-investigator assisting with the lab

research, contributing to data analysis and drafting some parts of the manuscript; RS: Co-investigator and participation in manuscript completion; DTA: Co-investigator assisting with the data analysis and paper editing; AD: participation in manuscript completion; YZ: Co-investigator assisting with the lab research.

References

An, F., Zhu, Y.F., Wei, S.N., & Li, S.C., 2013, An early Devonian to Early Carboniferous volcanic arc in North Tianshan, NW China: Geochronological and geochemical evidence from volcanic rocks: *Journal of Asian Earth Sciences*, **78**, 100–113.

An, F., Zhu, Y., Wei, S., & Lai, S., 2014, Geochronology and geochemistry of Shizishan sub-volcanic rocks in Jingxi-Yelmand gold deposit, north-west Tianshan: Its petrogenesis and implications to tectonics and au-mineralization. *Acta Petrologica Sinica*, **30**, 1545–1557.

An, F., & Zhu, Y.F., 2018, Geology and geochemistry of the Early Permian Axi low-sulfidation epithermal gold deposit in North Tianshan (NW China): *Ore Geology Reviews*, **100**, 12–30.

Barbarand, J., Hurford, T., & Carter, A., 2003, Variation in apatite fission-track length measurement: Implications for thermal history modelling: *Chemical Geology*, **198**, 77–106.

Biske, Y.S., & Seltmann, R., 2010, Paleozoic Tian-Shan as a transitional region between the Rheic and Urals – Turkestan oceans: *Gondwana Research*, **17**, 602–613.

Bobis, R.E., Jaireth, S., & Morrison, G.W., 1995, The anatomy of a Carboniferous epithermal ore shoot at Pajingo, Queensland: setting zoning, alteration and fluid conditions: *Economic Geology*, **90**, 1776–1798.

Chen, W., Liu, X.Y., & Zhang, S.H., 2002, Continuous laser stepwise heating $^{40}Ar/^{39}Ar$ dating technique: *Geological Review*, **48**, 127–134 (in Chinese with English abstract).

Chen, Y. J., Pirajno, F., Wu, G., Qi, J. P., & Xiong, X. L., 2011, Epithermal deposits in North Xinjiang, NW China: *International Journal of Earth Sciences*, **101**, 889–917.

Chen, Z.L., Wang , Z.X., Han, F.B., Zhang, W.G., Zhang, Q., Zhou, Z.J., Wang, X.H., Xiao, W.F., Han, S.Q., Yu, X.Q., Sun, Y., Nurgazy, T., Latyshev, N., & Zailabidin, H., 2017, Late Cretaceous–Cenozoic uplift, deformation, and erosion of the SW Tianshan Mountains in Kyrgyzstan and Western China: *International Geology Review*, DOI: 10.1080/00206814.2017.1365018.

Cherniak, D.J., & Watson, E.B., 2001, Pb diffusion in zircon: *Chemical Geology*, **172**, 5–24.

Cooke, D.R., & Simmons, S.F., 2000, Characteristics and Genesis of Epithermal Gold Deposits: *Reviews in Economic Geology*, **13**, 221–244.

Corbett, G.J., & Leach, T.M., 1998, Southwest Pacific Rim gold-copper systems: Structure, alteration and mineralization: *Society of Economic Geologists Special Publication*, **6**, 238–240.

De Grave, J., Buslov, M.M., & Van den haute, P., 2007, Distant effects of India–Eurasia convergence and Mesozoic intracontinental deformation in Central Asia: constraints from apatite fission-track thermochronology: *Journal of Asian Earth Sciences*, **29**, 188–204.

De Grave, J., Glorie, S., Buslov, M.M., Stockli, D.F., McWilliams, M.O., Batalev, V.Y., & Van Den Haute, P., 2013, Thermo-tectonic history of the Issyk-Kul basement (Kyrgyz northern Tien Shan, central Asia): *Gondwana Research*, **23**, 998–1020.

Downes, M., 2007, Yerranderie a Late Devonian silver–gold–lead intermediate sulfidation epithermal district, eastern Lachlan Orogen, New South Wales, Australia: *Resource Geology*, **57**, 1–23.

Galbraith, R.F., 1981, On statistical models for fission track counts: *Mathematical Geology*, **13**, 471–483.

Galbraith, R.F., & Laslett, G.M., 1993, Statistical models for mixed fission track ages: *Nuclear Tracks and Radiation Measurements*, **21**, 459–470.

Gallagher, K., Brown, R., & Johnson, C., 1998, Fission track analysis and its applications to geological problems: *Annual Review of Earth and Planetary Sciences*, **26**, 519–572.

Gao, J., Li, M., Xiao, X.Y., Tang, Y.Q., & He GQ., 1998, Paleozoic tectonic evolution of the Tianshan Orogen, northwestern China, *Tectonophysics*, **287(1)**, 213-231.

Gleadow, A.J.W., 1981, Fission-track dating method: what are the real alternatives: *Nuclear Track Detection*, **2**, 105–117.

Gleadow, A.J.W., Duddy, I.R., Green, P.F. & Lovering, J.F., 1986, Confined fission track lengths in apatite: a diagnostic tool for thermal history analysis: *Contributions to Mineralogy and Petrology*, **94**, 405–415.

Glorie, S., De Grave, J., Buslov, M.M., Elburg, M.A., Stockli, D.F., Gerdes, A., & Van der haute, P., 2010, Multi-method chronometric constraints on the evolution of the Northern Kyrgyz Tien Shan granitoids (Central Asian Orogenic Belt): From emplacement to exhumation: *Journal of Asian Earth Sciences*, **38**, 131–146.

Glorie, S., & De Grave, J., 2016, Exhuming the Meso–Cenozoic Kyrgyz Tianshan and Siberian Altai-Sayan: A review based on lowtemperature thermochronology: *Geoscience Frontiers*, **7**, 155–170.

Green, P.F., Duddy, I.R., Laslett, G.M., Hegarty, K.A., Gleadow, A.J.W., & Lovering, J.F., 1989, Thermal annealing of fission tracks in apatite 4. Quantitative modelling techniques and extension to geological timescales: *Chemical Geology*, **79**, 155–182.

Gu, X.X., Dong, L.H., Peng, Y.W., Wang, X.L., Yuan, P., & Zhu, B.Y., 2016, Formation and evolution of the epithermal–porphyry Au polymetallic mineralization system in the Tulasu volcanic basin of the West Tianshan, Xinjiang: *Acta Petrologica Sinica*, **32**, 1283–1300 (in Chinese with English abstract).

Han, B.F., He, G.Q., Wang, X.C., & Guo, Z.J., 2011, Late Carboniferous collision between the Tarim and Kazakhstan-Yili terranes in the western segment of the South Tian Shan Orogen, Central Asia, and implications for the Northern Xinjiang, western China: *Earth-Science Reviews*, **109**, 74–93.

Han, Y.G., & Zhao, G.C., 2018. Final amalgamation of the Tianshan and Junggar orogenic collage in the southwestern Central Asian Orogenic Belt: Constraints on the closure of the Paleo-Asian Ocean: *Earth-Science Reviews*, **186**, 129–152.

Hart, C.J.R., Wang, Y., Goldfarb, R.J., Begg, G., Mao, J.W., & Dong, L.H., 2003. Axi and associated epithermal gold deposits in western Tianshan, Xinjiang. Tectonic evolution and metallogeny of the Chinese Altay and Tianshan. In: Mao, J.W., Goldfarb, R.J., Seltman, R., Wang, D.H., Xiao, W.J., Hart, C.J.R., (eds) Tectonic evolution and

metallogeny of the Chinese Altay and Tianshan, IAGOD guidebook series **10**. *CERCAM/NHM*, London, pp 209–226.

Hedenquist, J.W., Arribas, A., & Gonzalez-Urien, E., 2000, Exploration for epithermal gold deposits: *Reviews in Economic Geology*, **13**, 245–277.

Hurford, A.J., & Green, P.F., 1983, The zeta-age calibration of fission track dating: *Chemical Geology*, **41**, 285–317.

Jepson, G., Glorie, S., Konopelko, D., Mirkamalov, R., Danišík, M., & Collins, A.S., 2018, The low-temperature thermo-tectonic evolution of the western Tian Shan, Uzbekistan: *Gondwana Research*, **64**, p. 122–136.

Jolivet, M., Dominguez, S., Charreau, J., Chen, Y., Li, Y.A., & Wang, Q.C., 2010, Mesozoic and Cenozoic tectonic history of the central Chinese Tian Shan: reactivated tectonic structures and active deformation: *Tectonics*, **29**, TC6019, https://doi.org/10.1029/2010TC002712.

Jolivet, M., Heilbronn, G., Robin, C., Barrier, L., Bourquin, S., Guo, Z.J., Jia, Y., Guerit, L., Yang, W., & Fu, B., 2013, Reconstructing the Late Palaeozoic–Mesozoic topographic evolution of the Chinese Tian Shan: available data and remaining uncertainties: *Advances in Geosciences*, **37**, 7–18.

Kerrich, R., Goldfarb, R.J., Groves, D.I., Garwin, S., & Jia, Y.F., 2000, The characteristics, origins and geodynamic settings of supergiant gold metallogenic provinces: *Science in China (Series D)*, **43**, 1–68.

Ketcham, R.A., 2005, Forward and inverse modeling of low-temperature thermochronometry data: *Reviews in Mineralogy and Geochemistry*, **58**, 275–314.

Ketcham, R.A., Carter, A., Donelick, R.A., Barbarand, J., & Hurford, A.J., 2007, Improved modeling of fission-track annealing in apatite: *American Mineralogist*, **92**, 799–810.

Koppers, A.A.P., 2002, ArArCALC—software for $^{40}Ar/^{39}Ar$ age calculations: *Computers & Geosciences*, **28**, 605–619.

Lehmann, B., Heinhorst, J., Hein, U., Neumann, M., Weisser, J.D., & Fedesejev, V., 1999, The Bereznjakovskoje gold trend, southern Urals, Russia: *Mineralium Deposita*, **34**, 241–249.

Liu, Z.K., Mao, X.C., Deng, H., Li, B., Zhang, S.G., Lai, J.Q., Bayless, R.C., Pan, M., Li, L.J., & Shang, Q.H., 2018, Hydrothermal processes at the Axi epithermal Au deposit, western Tianshan: insights from geochemical effects of alteration, mineralization and trace elements in pyrite: *Ore Geology Reviews*, **102**, 368–385.

Liu, Z.K., Mao, X.C., Ackerman, L., Li, B., Dick, J.M., Yu, M., Peng, J.T., & Shahzad, S.M., 2019, Two-stage gold mineralization of the Axi epithermal Au deposit, Western Tianshan, NW China: Evidence from Re-Os dating, S isotope, and trace elements of pyrite: *Mineralium Deposita*, **55**, 863–880.

Lomize, M., Demina, L., & Zarshchikov, A., 1997., The Kyrgyz-Terskei Paleoceanic Basin,Tien Shan: *Geotectonics*, **31**, 463–482.

McDougall, I., & Harrison, T.M., 1999, Geochronology and Thermochronology by the ^{40}Ar–^{39}Ar Method, second edition: Oxford, *Oxford University Press*, 269 p.

McInnes, B.I.A., Evans, N.J., Fu, F.Q., & Garwin, S., 2005, Application of thermochronology to hydrothermal ore deposits: *Reviews in Mineralogy and Geochemistry*, **58**, 467–498.

Mikolaichuk, A.V., Kurenkov, S.A., & Degtyarev, K.E., 1997, Main stages of geodynamic evolution of the North Tien Shan in the late Precambian and early Paleozoic: *Geotectonics*, **31 (6)**: 16–34.

Pang, J.Z., Zheng, D.W., Wan, J.L., Li, D.M., Zhang, P.Z., & Yang, J., 2013, Insufficient thermalization effects on determining fission track ages: *Science China*, **6**, 1233–1241.

Peng, Y.W., Gu, X.X., Lv, P.R., Zhang, Y.M., Cheng, W.B., & Wang, X.L., 2017, Genesis and tectonic setting of the Late Devonian Tawuerbieke gold deposit in the Tulasu ore cluster, western Tianshan, Xinjiang, China: *International Geology Review*, **59**, 1344–1368.

Pirajno, F., Seltmann, R., & Yang, Y., 2011. A review of mineral systems and associated tectonic settings of northern Xinjiang, NW China. *Geoscience Frontiers*, **2**, 157–185.

Ren, Q., Zhang, S., Wu, Y., Yang, T., Gao, Y., Turbold, S., Zhao, H., Wu, H., Li, H., Fu, H., Xu, B., Zhang, J., & Tomurtogoo, O., 2018a., New Late Jurassic to Early Cretaceous Paleomagnetic Results from North China and Southern Mongolia and Their Implications for the Evolution of the Mongol-Okhotsk Suture: *Journal of Geophysical Research: Solid Earth*, **123 (12)**, 10370–10398.

Ren, R., Han, B.F., Xu, Z., Zhou, Y.Z., Liu, B., Zhang, L., Chen, J.F., Su, L., Li, J., Li, X.H., & Li, Q.L., 2014, When did the subduction first initiate in the southern Paleo-Asian Ocean: New constraints from a Cambrian intra-oceanic arc system in West Junggar, NW China: *Earth and Planetary Science Letters*, **388**, 222–236.

Ren, R., Han, B.F., Guan, S.W., Liu, B., & Wang, Z.Z., 2018b, Linking the southern West Junggar terrane to the Yili Block: Insights from the oldest accretionary complexes in West Junggar, NW China: *Journal of Asian Earth Sciences*, **159**, 279–293.

Rui, Z., Goldfarb, R. J., Qiu, Y., Zhou, T., Chen, R., Pirajno, F., & Yun, G., 2002, Paleozoic–early Mesozoic gold deposits of the Xinjiang Autonomous Region, northwestern China: *Mineralium Deposita*, **37**, 393–418.

Schneider, J.W., Hoth, K., Gaitzsch, B.G., Berger, H.J., Steinborn, H., Walter, H., & Zeidler, M.K., 2005, Carboniferous stratigraphy and development of the Erzgebirge Basin, East Germany: *Zeitschrift der deutschen Gesellschaft für Geowissenschaften*, **156/3**, 431–466.

Schneider, J., & Romer, R.L., 2010, The Late Variscan Molasses (Late Carboniferous to Late Permian) of the Saxo-Thuringian Zone. In Linnemann, U. and Romer, R.L. (eds.) Pre-Mesozoic Geology of Saxo-Thuringia - *From the Cadomian Active Margin to the Variscan Orogen. Schweizerbart, Stuttgart*, 323–346.

Seltmann, R., Porter, T.M., & Pirajno, F., 2014, Geodynamics and metallogeny of the central Eurasian porphyry and related epithermal mineral systems: a review: *Journal of Asian Earth Sciences*, **79**, 810–841.

Sillitoe, R.H., & Hedenquist, J.W., 2003, Linkages between volcanotectonic settings, orefluid compositions, and epithermal precious metal deposits: *Society of Economic Geologists Special Publication*, **10**, 315–343.

Simmons, S.F., White, N.C., & John, D.A., 2005, Geological characteristics of epithermal precious and base metal deposits: *Economic Geology*, **100th Anniversary Volume**, 485–522.

Steiger, R.H., & Jäger, E., 1977, Subcommission on geochronology: convention on the use of

decay constants in geo- and cosmochronology: *Earth and Planetary Science Letters*, **36**, 359–362.

Tang, G. J., Wang, Q., Zhao, Z. H., Wyman, D. A., Chen, H. H., Jia, X. H., & Jiang, Z. Q., 2009, LA-ICP-MS zircon U–Pb geochronology, element geochemistry and petrogenesis of the andesites in the eastern Taerbieke gold deposit of the western Tianshan region. *Acta Petrologica Sinica*, **25**, 1341–1352 (in Chinese with English abstract).

Tang, G.J., Wang, Q., Wyman, D.A., Sun, M., Zhao, Z.H., & Jiang, Z.Q., 2013, Petrogenesis of gold-mineralized magmatic rocks of the Taerbieke area, northwestern Tianshan (western China): Constraints from geochronology, geochemistry and Sr-Nd-Pb-Hf isotopic compositions: *Journal of Asian Earth Sciences*, **74**, 113–128.

Ventura, B., & Lisker, F., 2003, Long-term landscape evolution of the northeastern margin of the Bohemian Massif: apatite fission-track data from the Erzgebirge (Germany): *International Journal of Earth Sciences*, **92**, 691–700.

Wainwright, A.J., Tosdal, R.M., Lewis, P.D., & Friedman, R.M., 2017, Exhumation and Preservation of Porphyry Cu-Au Deposits at Oyu Tolgoi, South Gobi Region, Mongolia: *Economic Geology*, **112(3)**, 591–601.

Wang, B., Faure, M., Cluzel, D., Shu, L. S., Charvet, J., & Meffre, S., 2006, Late Paleozoic tectonic evolution of the northern West Tianshan, NW China: *Geodinamica Acta*, **19**, 237–247.

Wang, S.S., 1983, Age determinations of ^{40}Ar–^{40}K, ^{40}Ar–^{39}Ar and radiogenic ^{40}Ar released characteristics on K–Ar geostandards of China: *Chinese Journal of Geology*, **4**, 315–323 (in Chinese with English abstract).

Wang, Y.N., Cai, K.D., Sun, M., Xiao, W.J., De Grave, J., Wan, B., & Bao, Z.H., 2018, Tracking the multi-stage exhumation history of the western Chinese Tianshan by apatite fission track (AFT) dating: Implication for the preservation of epithermal deposits in the ancient orogenic belt: *Ore Geology Reviews*, **100**, 111–132.

Wei, J.L., Cao, X.Z., Wang, Q.F., & Han, J.M., 2011, Typomorphic characteristics and geological significance of the pyrites from Axi gold deposit, Xinjiang, China: *Geological Science and Technology Information*, **31**, 89–96 (in Chinese with English abstract).

Windley, B.F., Alexeiev, D., Xiao, W.J., Kröner, A., & Badarch, G., 2007, Tectonic models for accretion of the Central Asian Orogenic Belt: *Journal of the Geological Society*, **164**, 31–47.

Wolff, R., Dunkl, I., Lange, J.-M., Tonk, C., Voigt, T. & von Eynatten, H., 2015, Superposition of burial and hydrothermal events: post-Variscan thermal evolution of the Erzgebirge, Germany: *Terra Nova*, **27**, 292–299.

XBGMR, 1993, Regional geology of Xinjiang Uygur Autonomy Region: Beijing, *Geological Publishing House*, 841 p (in Chinese).

Xiao, W.J., Windley, B.F., Allen, M., & Han, C.M., 2013, Paleozoic multiple accretionary and collisional tectonics of the Chinese Tianshan orogenic collage: *Gondwana Research*, **23**, 1316–1341.

Xiao, W.J., Windley, B. F., Sun, S., Li, J., Huang, B., Han, C., Yuan, C., Sun, M., & Chen, H., 2015, A Tale of Amalgamation of Three Permo-Triassic Collage Systems in Central Asia: Oroclines, Sutures, and Terminal Accretion: *Annual Review of Earth and*

Planetary Sciences, **43**, 477–507.

Xiao, X.C., Tang, Y.Q., Feng, Y.M., Zhu, B.Q., Li, J.Y., & Zhao, M., 1992, Tectonic evolution of Northern Xinjiang and its adjacent regions: Beijing, *Geological Publishing House*, 169 p (in Chinese).

Xu, X.Y., Xia, L.Q., Ma, Z.P., Wang, Y.B., Xia, Z.C., Li, X.M., & Wang, L.S., 2006, SHRIMP zircon U–Pb geochronology of the plagiogranites from Bayingou ophiolite in North Tianshan Mountains and the petrogenesis of the ophiolite: *Acta Petrologica Sinica*, **22**, 83–94 (in Chinese with English abstract).

Xue, C.J., Zhao, X.B., Mo, X.X., Dong, L.H., Gu, X.X., Nurtaev, B., Pak, N., Zhang, Z.C., Wang, X.L., Zu, B., Zhang, G.Z., Feng, B., & Liu, J.Y., 2014, Asian Gold Belt in western Tianshan and its dynamic settings, metallogenic control and exploration: *Earth Science Frontiers*, **21**, 128–155 (in Chinese with English abstract).

Yang, Y.T., Guo, Z.X., Song, C.C., Li, X.B., & He, S., 2015., A short but significant Mongol-Okhotsk collisional orogeny in latest Jurassic-earliest Cretaceous: *Gondwana Research*, **28 (3)**, 1096–1116.

Yin, A., & Harrison, T.M., 2000., Geological evolution of the Himalayan-Tibetan orogen: *Annual Review in Earth and Planetary Sciences*, **28**, 211–280.

Yu, X., Wang, Z., Zhou, X., Xiao, W., & Yang, X., 2016, Zircon U–Pb geochronology and Sr–Nd isotopes of volcanic rocks from the Dahalajunshan Formation: implications for Late Devonian–Middle Carboniferous tectonic evolution of the Chinese Western Tianshan: *International Journal of Earth Sciences*, **105**, 1637–1661.

Zhai, W., Sun, X.M., Sun, W.D., Su, L.W., He, X.P., & Wu, Y.L., 2009, Geology, geochemistry, and genesis of Axi: A Paleozoic low-sulfidation type epithermal gold deposit in Xinjiang, China: *Ore Geology Reviews*, **36**, 265–281.

Zhang, B., Chen, W., Liu, J.Q., Yin, J.Y., & Sun, J.B., 2019, Thermochronological insights into the intracontinental orogeny of the Chinese western Tianshan orogen: *Journal of Asian Earth Sciences*, https://doi.org/10.1016/j.jseaes.2019.103927.

Zhang, B., Li, N., Shu, S.P., Wang, W., Yu, J., Chen, X., Ye, T., & Chen, Y.J., 2018, Textural and compositional evolution of Au-hosting Fe-S-As minerals at the Axi epithermal gold deposit, Western Tianshan, NW China: *Ore Geology Reviews*, **100**, 31–50.

Zhao, W.C., Zhao, X.B., Xue, C.J., Symon, D.T.A., Cui, X.J., & Xing, L., 2019., Structural characterization of the Katebasu gold deposit, Xinjiang, China: Tectonic correlation with the amalgamation of the western Tianshan: *Ore Geology Reviews*, **107**: 888–902.

Zhao, X.B., Xue, C.J., Chi, G.X., Wang, H.G., & Qi, T.J., 2014a, Epithermal Au and polymetallic mineralization in the Tulasu Basin, western Tianshan, NW China: Potential for the discovery of porphyry Cu–Au deposits: *Ore Geology Review*, **60**, 76–96.

Zhao, X.B., Xue, C.J., Men, Q.H., Yan, Y.H., Wang, H.G., Zu, B., Mi D.J., & Li, X.Z., 2014b, Origin and metallogenesis of the Tawuerbieke gold deposit, western Tianshan: Insight from Re–Os geochronology and S–Pb isotopic compositions: *Earth Science Frontiers*, **21**, 176–186 (in Chinese with English abstract).

Zhao, X.B., Xue, C.J., Symons, D.T.A., Zhang, Z.C., & Wang, H.G., 2014c, Microgranular enclaves in island–arc andesites: A possible link between known epithermal Au and potential porphyry Cu–Au deposits in the Tulasu ore cluster, western Tianshan, Xinjiang,

China: *Journal of Asian Earth Sciences*, **85**, 210–223.

Zhao, X. B., Xue, C. J., Seltmann, R., Dolgopolova, A., Andersen, J. C., & Zhang, G. Z., 2020, Volcanic-plutonic connection and associated Au-Cu mineralization of the Tulasu ore district, Western Tianshan, NW China: Implications for mineralization potential in Paleozoic arc terranes. *Geological Journal*, **55**, 2318–2341.

Zonenshain, L.P., Kuzmin, M.I., & Natapov, L.M., 1990, Geology of the USSR: A plate tectonic synthesis: American Geophysical Union, *Geodynamics Series*, **21**, 242 p.

Figure Captions

Fig. 1. (A) Schematic map of the Central Asian Orogenic Belt (modified from Han *et al.* 2011). (B) Tectonic divisions of the western Tianshan orogen (modified from Xue *et al.* 2014), showing the distribution of major gold deposits.

Fig. 2. Simplified geological map of the Tulasu epithermal gold district (modified from Zhao *et al*. 2014*a*).

Fig. 3. Stratigraphic sections of the Upper Paleozoic sequences of the Tulasu epithermal gold district, showing the spatial and temporal framework and volcanic assemblages of the DVF (Zhao *et al*. 2020).

Fig. 4. K-feldspar $^{40}Ar/^{39}Ar$ plateau age spectrum of monzonite porphyry enclave (# XT4-8) from the Tulasu epithermal gold district.

Fig. 5. Radial plots of single-grain apatite fission track ages for each sample in the Tulasu epithermal gold district. X-axis = relative errors of single grain ages (inversely related to precision, expressed as percentages); Y-axis = standard estimates on single grain ages; arc axis = single grain ages; n = number of apatite grains dated.

Fig. 6. Length histograms for the apatite fission tracks from the Tulasu epithermal gold system. Abbreviations: MTL = mean track length; N = number of horizontally-confined fission-track lengths measured.

Fig. 7. Modelled time–temperature path envelopes and weighted mean paths of samples from the Tulasu epithermal gold system, on the basis of apatite fission track data. Abbreviation: APAZ = apatite partial annealing zone.

Fig. 8. Integrated geochronological and thermochronological data revealing the cooling and exhumation histories of the Tulasu epithermal gold system. Abbreviations: AFT = apatite fission track; Kfs Ar/Ar = K-feldspar $^{40}Ar/^{39}Ar$; Zrn U–Pb = zircon U–Pb.

Fig. 9. Apatite fission track (AFT) age versus elevation plot for the volcanic rock samples in the Tulasu basin. The red dashed line represents a negative linear relation between AFT ages and elevations after discarding the sample QBK-1 with extremely younger AFT age.

Table Captions

Table 1. *Main characteristics of the epithermal deposits in the Tulasu volcanic basin.*

Table 2. *Locations and descriptions of samples used for this study.*

Table 3. *Results of K-feldspar $^{40}Ar/^{39}Ar$ dating in the Tulasu epithermal gold district.*

Table 4. *Results of apatite fission track dating of volcanic rocks in the Tulasu epithermal gold district.*

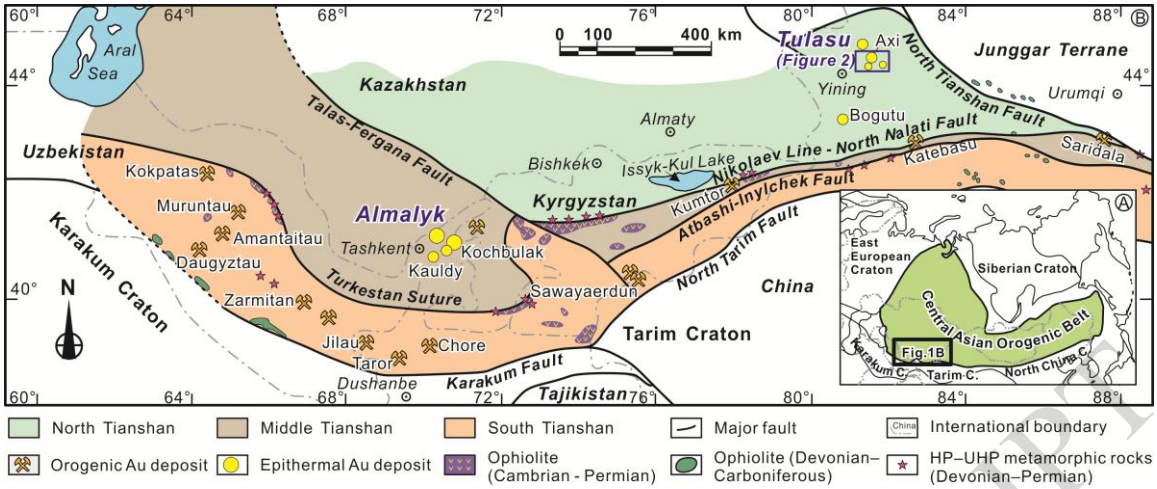

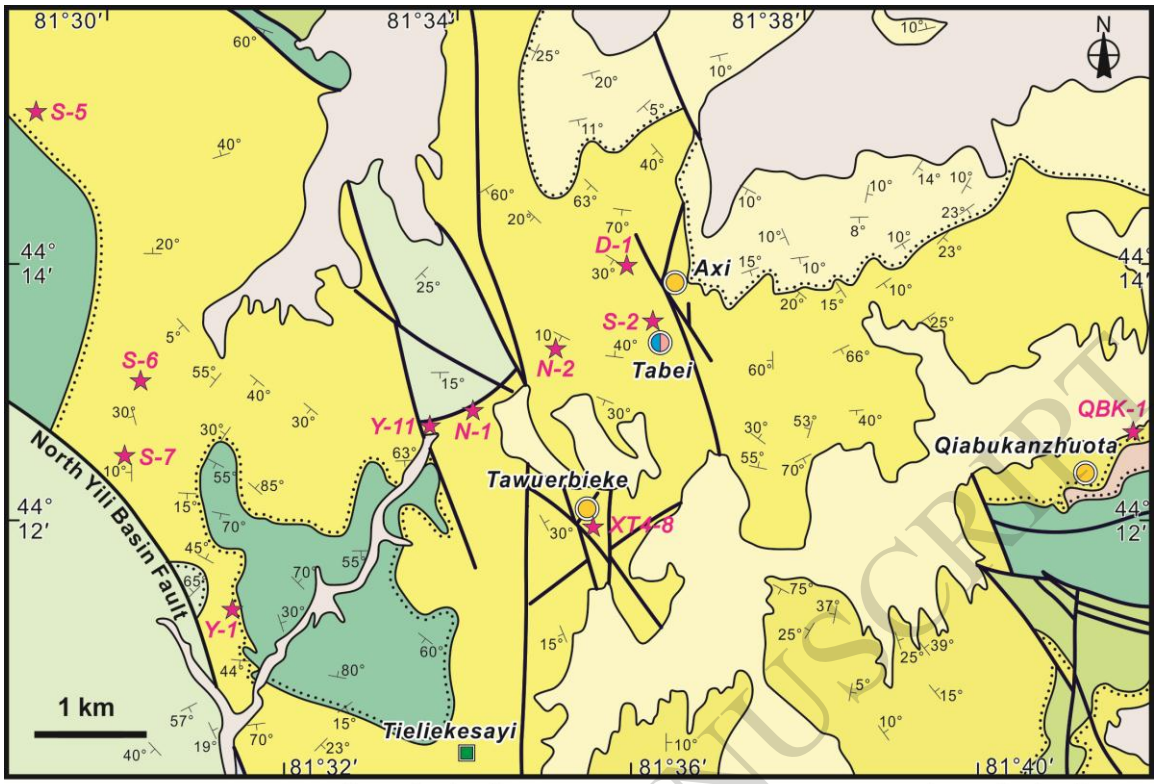

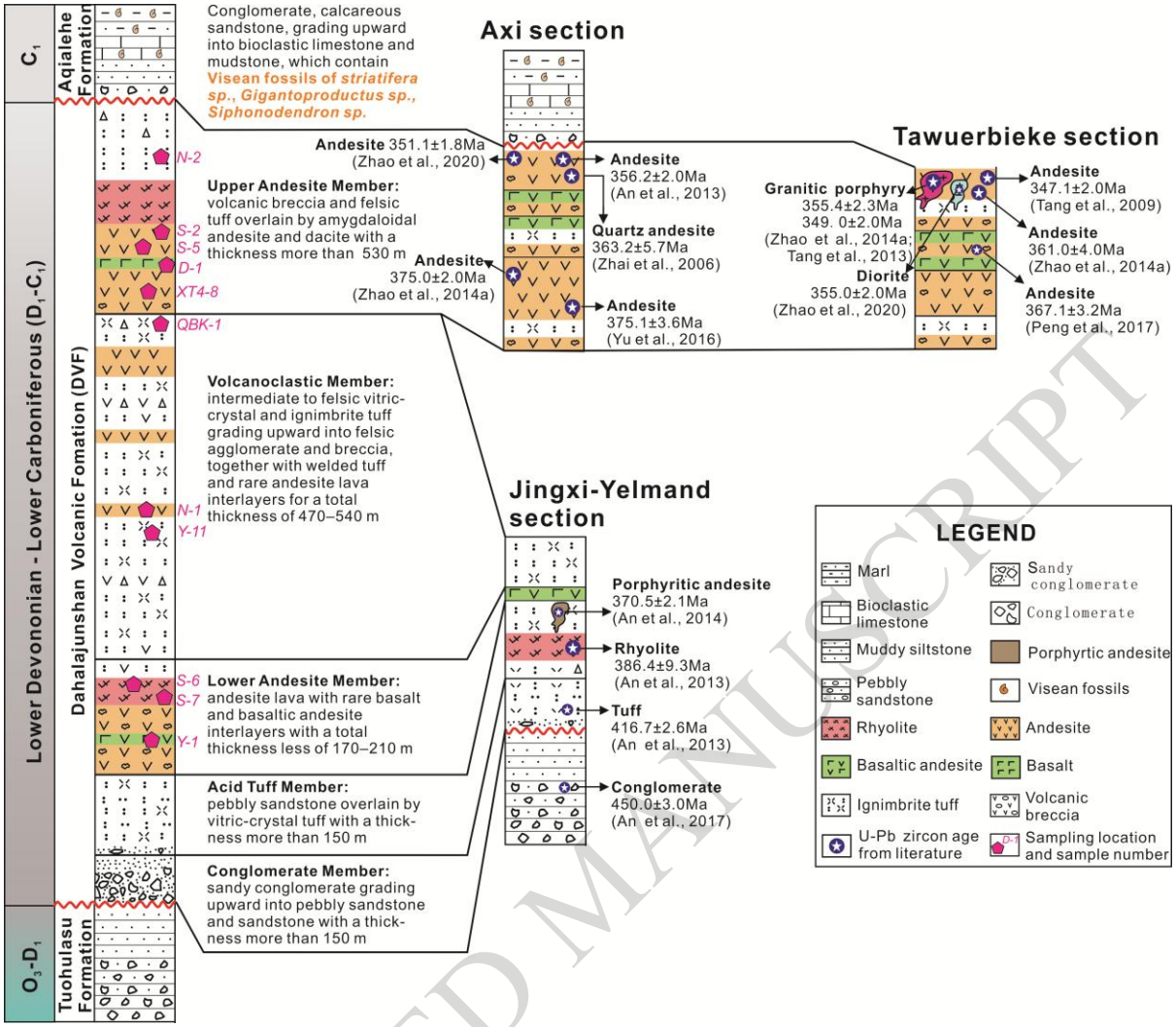

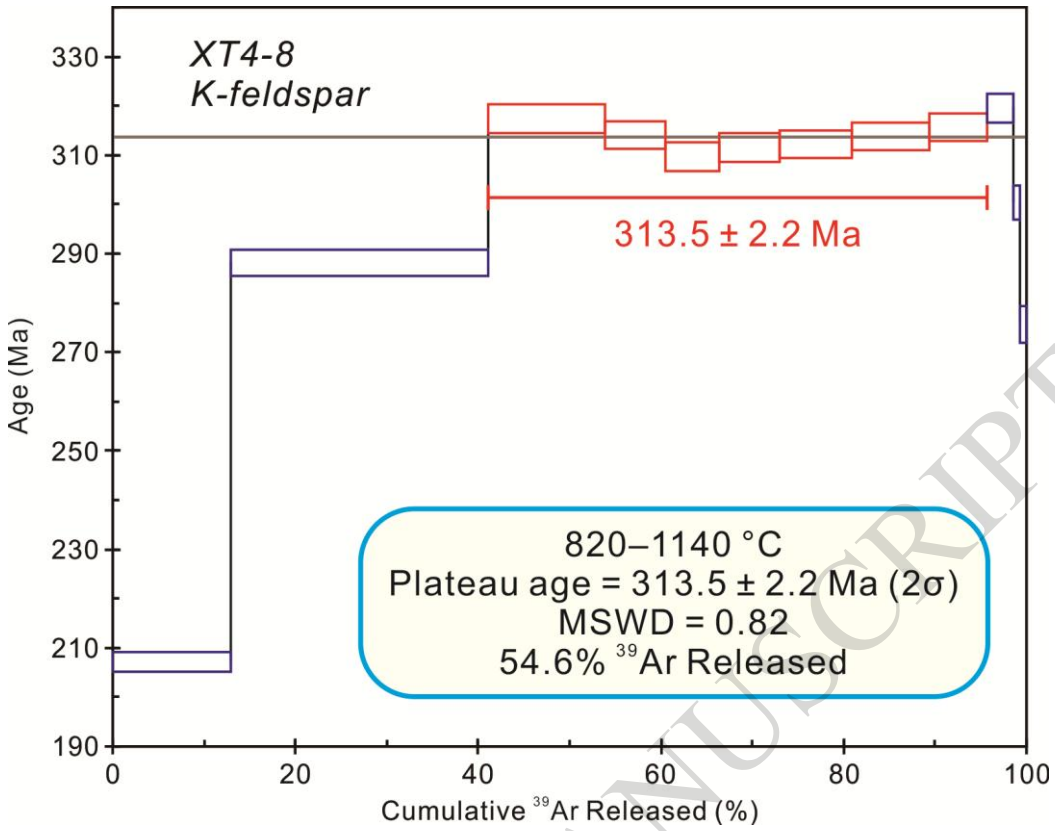

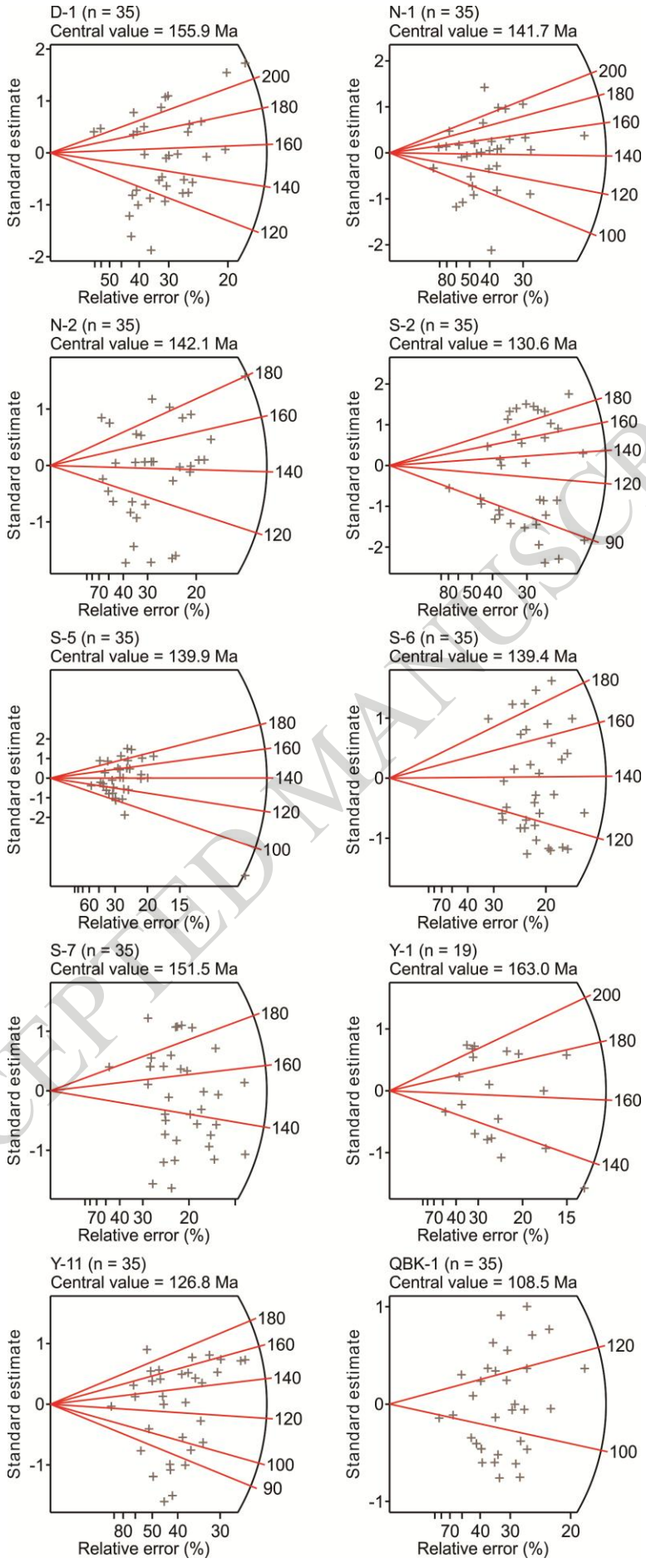

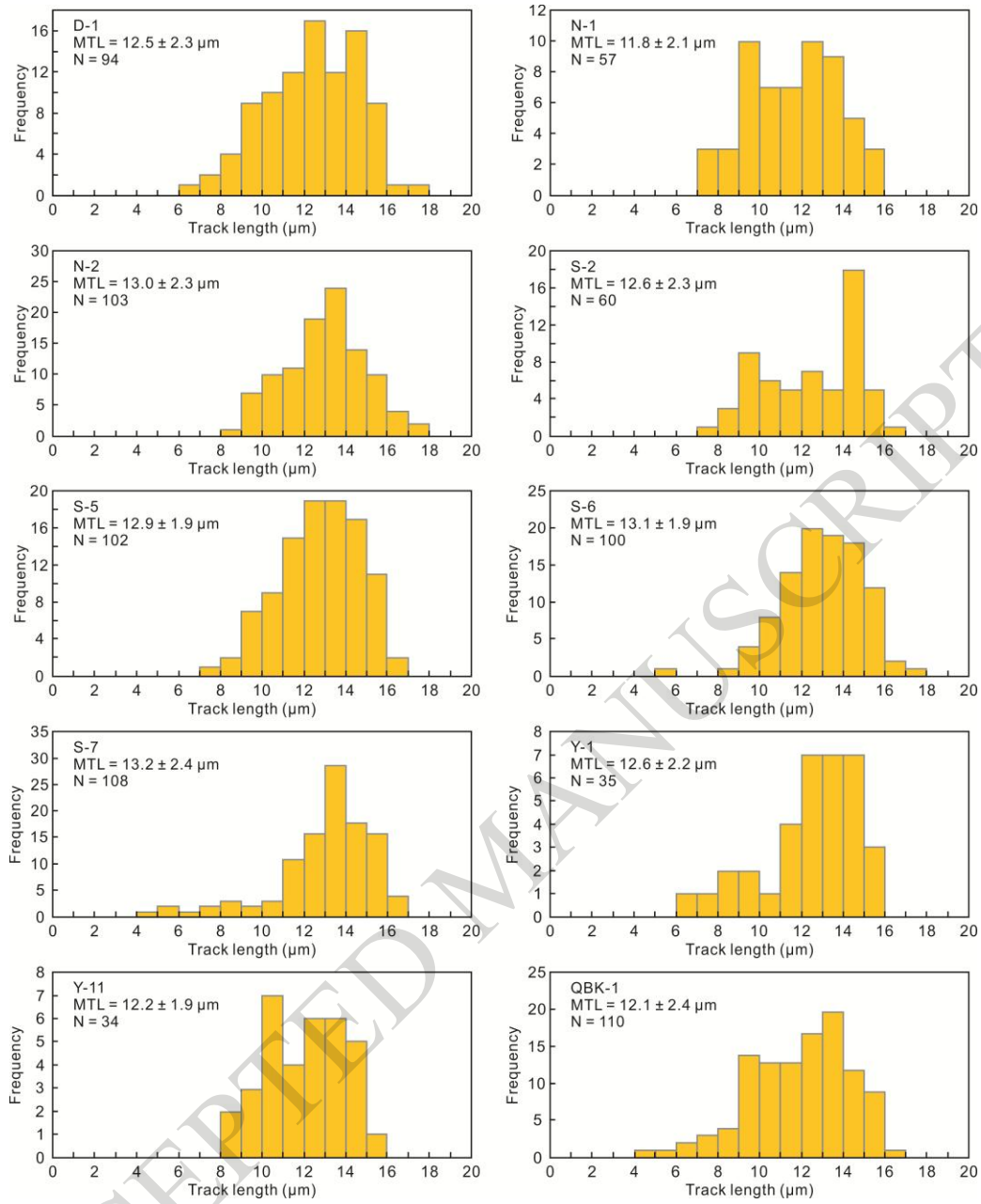

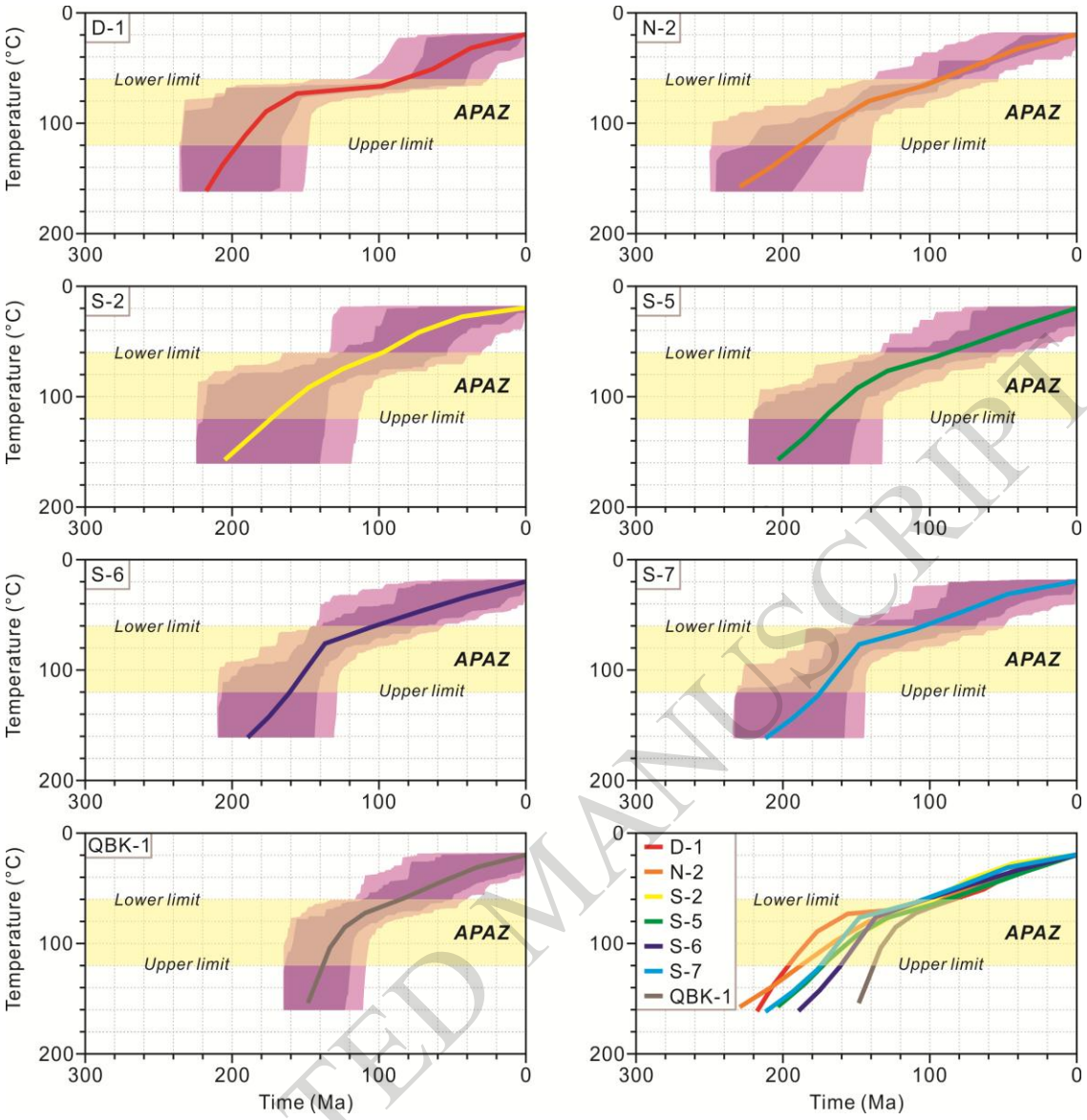

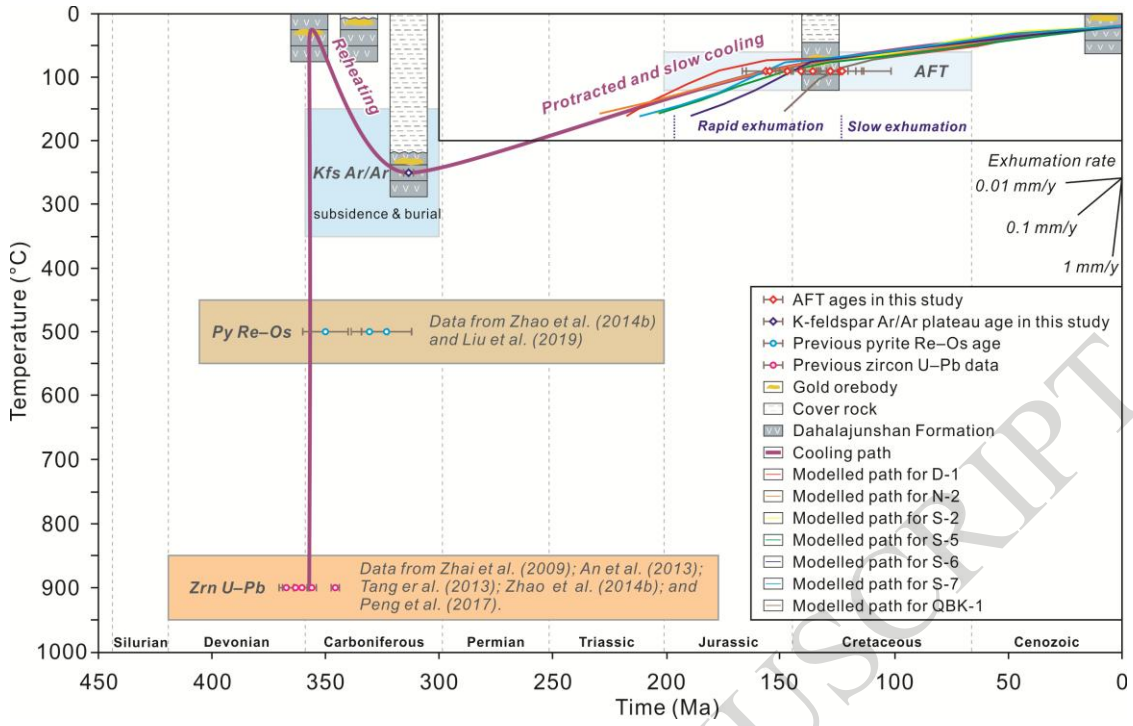

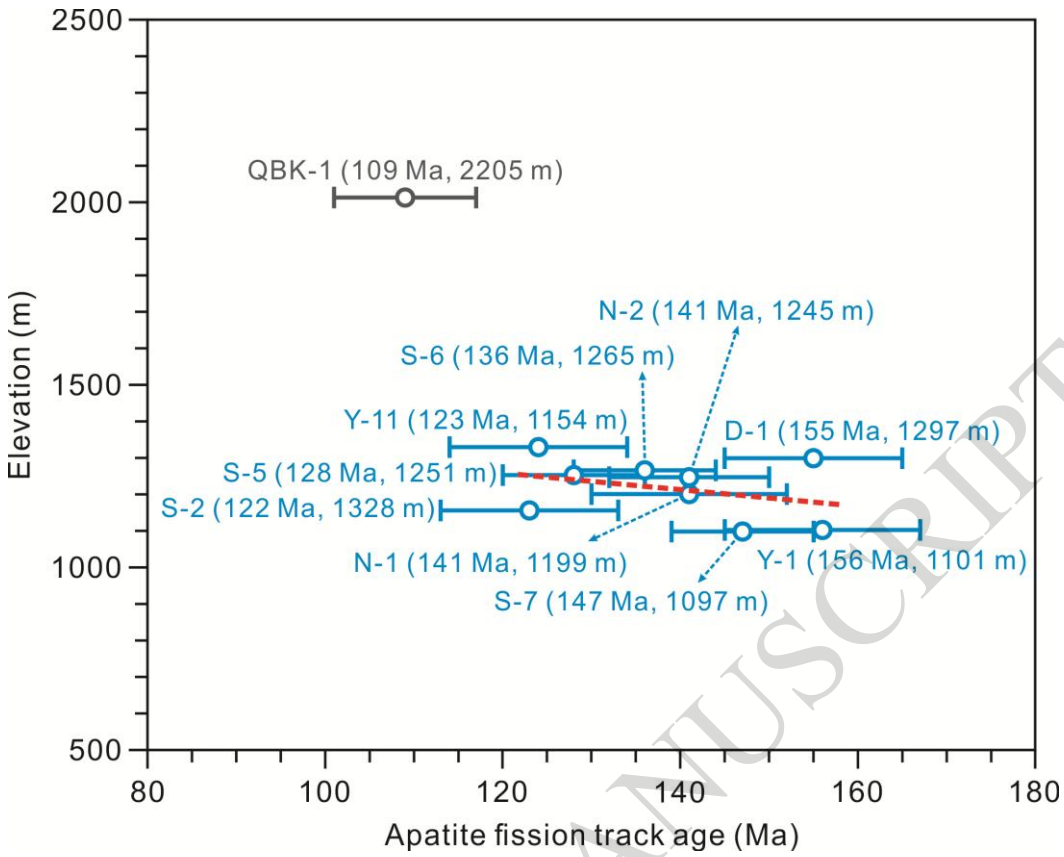

Table 1. *Main characteristics of the epithermal deposits in the Tulasu volcanic basin.*

Ore deposit	Axi Au	Tawuerbieke Au	Qiabukanzhuota Au	Tabei Pb–Zn
Coordinates	N 44.2341, E 81.6083	N 44.2072, E 81.6063	N 44.2161, E 81.7016	N 44.2241, E 81.6044
Size (t)	70	Small	Prospect	Prospect
Grade	3–8 g/t	1.2–32.5 g/t	0.5–2.0 g/t	Pb 2.82%; Zn 6.03%
Host Rock	Andesitic rocks	Andesitic rocks, tuff and granitic porphyry	Dacite and tuff	Tuff
Ore-controlling Structure	N–S fault	NNW–SSE and N–S faults	NE–SW fracture zone	N–S fault
Orebody Shape	Lenticular and vein-like	Lenticular and vein-like	Lenticular and stratiform	Lenticular and vein-like
Ore Type	Quartz vein, altered rock and breccia	Altered rock and calcite–quartz vein	Silicified breccia and silicified tuff	Massive, breccia and banded
Ore Mineral	Pyrite, arsenopyrite, electrum and marcasite	Pyrite, minor electrum and native gold	Pyrite, chalcopyrite	Sphalerite, galena and minor chalcopyrite
Gangue Mineral	Chalcedony, quartz, sericite, calcite and adularia	Calcite, sericite, quartz and chlorite	Quartz, kaolinite and sericite	Quartz, gypsum, calcite and chlorite
Hydrothermal Alteration	Silicification, phyllic and propylitization	Silicification, sericite, chlorite and carbonate	Silicification and sericite	Silicification, kaolinite and chlorite
Reference	Zhai *et al*. (2009); Zhao *et al*. (2014*a*); Liu *et al*. (2018)	Zhao *et al*. (2014a, *b*); Peng *et al*. (2017)	Zhao *et al*. (2014*a*)	Zhao *et al*. (2014*a*); Gu *et al*. (2016)

Table 2. *Locations and descriptions of samples used for this study.*

Sample no.	Description	Mineral Dated	Latitude (N), Longitude (E)	Elevation
XT4-8	Monzonite porphyry enclave hosted in andesite from the DVF	K-feldspar	44°12′02″, 81°36′16″	1886 m
D-1	Basaltic andesite of the Upper Andesite member from the DVF	Apatite	44°13′59″, 81°35′58″	1297 m
N-1	Andesite of the Volcanoclastic member from the DVF	Apatite	44°12′53″, 81°34′12″	1199 m
N-2	Tuff of the Upper Andesite member from the DVF	Apatite	44°13′20″, 81°35′03″	1245 m
S-2	Andesite of the Upper Andesite member from the DVF	Apatite	44°13′33″, 81°36′16″	1328 m
S-5	Andesite of the Upper Andesite member from the DVF	Apatite	44°15′11″, 81°29′11″	1251 m
S-6	Andesite of the Lower Andesite member from the DVF	Apatite	44°13′05″, 81°30′23″	1265 m
S-7	Dacite of the Lower Andesite member from the DVF	Apatite	44°12′30″, 81°30′12″	1097 m
Y-1	Basaltic andesite of the Lower Andesite member from the DVF	Apatite	44°11′18″, 81°31′40″	1101 m
Y-11	Rhyolite of the Volcanoclastic member from the DVF	Apatite	44°12′45″, 81°33′41″	1154 m
QBK-1	Tuff of the Volcanoclastic member from the DVF	Apatite	44°12′56″,81°41′47″	2011 m

Table 3. *Results of K-feldspar $^{40}Ar/^{39}Ar$ dating in the Tulasu epithermal gold district.*

T (°C)	$(^{40}Ar/^{39}Ar)_m$	$(^{36}Ar/^{39}Ar)_m$	$(^{37}Ar/^{39}Ar)_m$	$(^{38}Ar/^{39}Ar)_m$	^{40}Ar (%)	F	^{39}Ar ($\times10^{-14}$ mol)	Accumulated ^{39}Ar (%)	Age (Ma)	±1σ (Ma)
700	41.1847	0.0563	0.0073	0.0235	59.61	24.5486	2.76	12.94	207.2	2.0
770	37.4537	0.0085	0.0067	0.0137	93.30	34.9435	6.00	41.02	288.2	2.7
820	40.2127	0.0048	0.0042	0.0131	96.49	38.8019	2.75	53.89	317.4	2.9
870	40.4110	0.0069	0.0000	0.0139	94.95	38.3718	1.40	60.47	314.1	2.9
920	40.4011	0.0089	0.0000	0.0147	93.48	37.7672	1.23	66.40	309.6	2.9
970	41.0374	0.0102	0.0000	0.0146	92.66	38.0256	1.41	73.00	311.5	2.9
1020	41.5282	0.0115	0.0174	0.0151	91.79	38.1179	1.69	80.90	312.2	2.9
1080	41.4877	0.0107	0.0125	0.0148	92.40	38.3343	1.81	89.38	313.8	2.9
1140	40.9777	0.0081	0.0000	0.0145	94.16	38.5849	1.34	95.64	315.7	2.9
1200	41.7876	0.0091	0.0108	0.0139	93.58	39.1060	0.62	98.55	319.6	3.0
1300	42.5212	0.0202	0.0000	0.0175	85.84	36.5422	0.16	99.30	300.3	3.5
1400	42.5187	0.0031	0.0000	0.0164	78.35	33.3151	0.15	100.00	275.7	3.8

Sample weight = 26.24 mg; Heating step = 12; Irradiation parameter = 0.004957; T = temperature;
F = $^{40}Ar^*/^{39}Ar$, is the ratio of radiogenic ^{40}Ar and ^{39}Ar.

Table 4. *Results of apatite fission track dating of volcanic rocks in the Tulasu epithermal gold district.*

Sample	n	ρ_s (10^5/cm^2) (N_s)	ρ_i (10^5/cm^2) (N_i)	ρ_d (10^5/cm^2) (N_d)	P (χ^2) (%)	Central Age (Ma)(± 1σ)	Pooled Age (Ma)(± 1σ)	Mean Track Length (μm) (N)
D-1	35	4.377 (679)	6.163 (956)	10.769 (6313)	83.3	155 ± 10	155 ± 10	12.5 ± 2.3 (94)
N-1	35	4.263 (422)	4.738 (469)	7.718 (6313)	99.1	141 ± 11	141 ± 11	11.8 ± 2.1 (57)
N-2	35	4.266 (969)	4.376 (994)	7.145 (6313)	81.3	141 ± 9	141 ± 9	13.0 ± 2.3 (103)
S-2	35	5.957 (664)	10.101 (1126)	10.197 (6313)	1.2	124 ±10	122 ± 8	12.6 ± 2.3 (60)
S-5	35	4.707 (936)	7.322 (1456)	9.815 (6313)	9.3	135 ± 9	128 ± 8	12.9 ± 1.9 (102)
S-6	35	6.021 (1346)	8.46 (1891)	9.434 (6313)	82.1	136 ± 8	136 ± 8	13.1 ± 1.9 (100)
S-7	35	6.425 (1495)	8.033 (1869)	9.052 (6313)	93.3	147 ± 8	147 ± 8	13.2 ± 2.4 (108)
Y-1	19	7.601 (591)	11.549 (898)	11.722 (6313)	95.2	156 ± 11	156 ± 11	12.6 ± 2.2 (35)
Y-11	35	4.131 (320)	10.328 (800)	15.155 (6313)	97.8	123 ± 10	123 ± 10	12.2 ± 1.9 (34)
QBK-1	35	5.019 (598)	7.479 (891)	7.999 (6039)	100.0	109 ± 8	109 ± 8	12.1 ± 2.4 (110)

n = number of apatite grains dated; ρ_s and N_s = spontaneous fission track density on the internal surfaces of apatite grains and the corresponding total number of fission tracks measured; ρ_i and N_i = induced fission track density on the muscovite external detector and the corresponding total number of fission tracks measured; ρ_d and N_d = induced fission track density on the monitor dosimeter glasses and the corresponding total number of fission tracks measured; P (χ^2) = chi-square probability that all single grain ages represent a single age population where the degrees of freedom = Nc - 1 (Galbraith, 1981); N = total number of horizontally-confined fission track lengths measured for apatite grains.